Spatiotemporal antiresonance in coupled reaction-diffusion systems

Krishnendu Pal, Shibashis Paul, and Deb Shankar Ray*
Indian Association for the Cultivation of Science, Jadavpur, Kolkata 700032, India

(Received 28 November 2019; accepted 17 April 2020; published 5 May 2020)

We present a theoretical study of the spatiotemporal antiresonance in a system of two diffusively coupled chemical reactions, one of which is driven by an external periodic forcing. Although antiresonance is well known in various physical systems, the phenomenon in coupled chemical reactions has largely been overlooked. Based on the linearized dynamics around the steady state of the two-component coupled reaction-diffusion systems we have derived the general analytical expressions for the amplitude-frequency response functions of the driven and undriven components of the system. Our theoretical analysis is well corroborated by detailed numerical simulations on coupled Gray-Scott reaction-diffusion systems exhibiting antiresonance dip in the amplitude-frequency response curve as a result of destructive interference between the coupling and the periodic external forcing imparting differential stability of the two subsystems. This leads to the emergence of spatiotemporal patterns in an undriven subsystem, while the driven one settles down to a homogeneously stable steady state.

DOI: 10.1103/PhysRevE.101.052203

I. INTRODUCTION

The phenomenon of antiresonance has been a topic of interest in physical and engineering sciences over the past several decades. It is now well established that when any one of the oscillators is driven by external periodic force in a system of N number of coupled linear oscillators the response of the particular oscillator being forced, for certain types of coupling interaction, displays $(N-1)$ number of antiresonance dips in the response amplitude-frequency spectrum [1–3] along with maximum N number of resonance maxima alternatively, depending on the values of the parameters [2,4]. Antiresonance has also been observed in nonlinear systems [4,5] and proved to be useful when the system is expected to deliver low signal output. Unlike resonance which depends on all the components of the oscillators in the assembly and on their coupling, the antiresonance solely depends on the characteristics of the oscillator being driven and not the other coupled oscillators [5]. Therefore, this has served as an important tool for gaining information about the individual oscillators by driving them individually in a complex assembly of systems which cannot easily be separated into their constituent components [6]. Several variants of the phenomenon, such as parametric antiresonance, stochastic antiresonance, and coherence antiresonance, have been proposed over the past few years [4]. Antiresonance has also been observed in quantum oscillators [7,8], in cavity electrodynamics [9], in a quintic oscillator [10], and in quantum dot [11] and been exploited to demonstrate desynchronizing undesired oscillations [12], driving microelectronic motor [13], dynamic model updating [14], and vibration control [15]. Further applications of antiresonance in wave traps in radio receivers [16], electrical circuits [17], structural analysis [6,18], mechanical engineering [19], chemotherapeutic protocols [20], etc. are reported. Recently, antiresonance has been used to study excitable biological systems, such as Hodgkin-Huxley neuron [21], in single-molecule thiophene junctions [22] and cavity antiresonance spectroscopy of dipole coupled subradiant arrays [23].

The aim of the present paper is a systematic study of antiresonance in coupled reaction-diffusion systems. The major motivation stems from the numerical and experimental investigations on multilayer coupled systems since they provide prototypical examples in the biological world, particularly, in neural, developmental, and ecological contexts [24] under a far from equilibrium condition [25]. The research on layered structures has become popular since the past decade [26] in the context of Brusselator model [27], Gierer-Meinhardt [28,29], three-component reaction-diffusion model [30], and CDIMA and BZ reactions [24,31,32]. Simulations using the coupled Oregonator model have revealed twinkling eye patterns, Turing spots arranged in a hexagonal lattice, pinwheels in spots, and traveling waves in labyrinths [33,34]. Studies on coupled layers have been also extended to drug delivery studies [35] and networks of reaction-diffusion systems [36].

Keeping in view of the aforesaid development of the coupled layer dynamics of reaction-diffusion systems, we now look for antiresonance when one of the systems is externally driven [37]. To bring the issue into an appropriate perspective we first note that since antiresonance arises as a result of destructive interference between coupling and the driving force, the interference may in turn induce a difference in stability of the two constituents of the coupled system. Our objective here is to understand this interference-induced differential instability of the spatiotemporal dynamics of the coupled reaction-diffusion systems. In what follows we consider a reaction-diffusion system in two layers which are transversely coupled minimally and the system in one of the layers is externally driven by a sinusoidal time-varying term. The external drive may be a controlled light source [34,38] if one

*Corresponding author: pcdsr@iacs.res.in

 ©2020 American Physical Society

of the components is photosensitive [32,39] or a source term for the substrate injection [40]. Our primary focus here is to tune the frequency of the single external periodic drive to control the interference between this forcing and coupling. It has been shown that this destructive interference has a direct bearing on the dynamical response of the coupled system in two layers which is manifested in spatiotemporal antiresonance. This is reflected in the formation of nonstationary patterns in the undriven layer, while the system in the driven layer settles down to a homogeneous steady state. Based on linear stability analysis we have derived the general expressions for amplitude-frequency response functions for the driven and undriven components of the system. An explicit example using the Gray-Scott [41] reaction has been worked out in detail to demonstrate the antiresonance dip in between the two resonance maxima in the response curve for the driven layer. Finally, full-scale numerical simulation on the coupled dynamics has been performed to verify the theoretical prediction on spatiotemporal antiresonance.

The layout of the paper is organized as follows. In Sec. II we have presented a theoretical analysis of spatiotemporal antiresonance in coupled reaction-diffusion systems on a general footing. Using the Gray-Scott reaction-diffusion system as an example we have shown that the linear analysis predicts spatiotemporal antiresonance in Sec. III. Detailed numerical simulations have been performed to demonstrate nonstationary spatial patterns for the undriven layer, while the driven layer reduces to a homogeneous steady state. The paper is concluded in Sec. IV.

II. SPATIOTEMPORAL ANTIRESONANCE IN COUPLED CHEMICAL REACTIONS: THEORETICAL CONSIDERATIONS

In the first half of this section we show how the linearized dynamics of the two transversely coupled chemical reaction-diffusion systems around a homogeneous steady state can be represented as two coupled physical oscillators in the presence of an external periodic forcing. Subsequently the expressions for the amplitude-frequency response functions of two components are derived.

A. Linear analysis of transversely coupled reaction-diffusion systems as coupled oscillators

We begin with two identical coupled layers, each with two components, $u(x, y)$ and $v(x, y)$, of the reaction-diffusion system in two dimensions (x, y) (denoted by r) as follows:

$$\dot{u_1}(r,t) = F_1(u_1, v_1) + D_u\nabla_r^2 u_1 + \alpha(u_2 - u_1) + (2G_0)\sin(\omega t), \tag{2.1}$$

$$\dot{v_1}(r,t) = G_1(u_1, v_1) + D_v\nabla_r^2 v_1, \tag{2.2}$$

$$\dot{u_2}(r,t) = F_2(u_2, v_2) + D_u\nabla_r^2 u_2 + \alpha(u_1 - u_2), \tag{2.3}$$

$$\dot{v_2}(r,t) = G_2(u_2, v_2) + D_v\nabla_r^2 v_2, \tag{2.4}$$

where the overdot expressions on the left hand side of the equations describe the time derivative of the concentration of the respective components; the functions $F_i(u_i, v_i)$ and $G_i(u_i, v_i)$ (where $i = 1$ denotes the top layer and $i = 2$ denotes the bottom layer or the second layer) describe their reaction kinetics whose functional form depends on the specific chemical reaction under consideration. As we consider the identical layers the functional forms of F_1 and F_2 are the same; the same is true for G_1 and G_2. The terms having Laplacian operator ($\nabla_r^2 = \frac{\partial^2}{\partial x} + \frac{\partial^2}{\partial y}$) describe the lateral diffusion of the components along x and y directions and the terms involving the coupling constant α, between the two layers, denote the vertical (along z axis, the interlayer separation is negligibly small) or transversal diffusion. $u_i(r, t)$ and $v_i(r, t)$ are the field variables or the chemical concentrations at the spatial coordinate (x, y) at time t. The external periodic forcing term can be thought of as an intelligent modulator or a source term which periodically supplies in and also extracts out the u_1 component from the top layer. Here $2G_0$ is the amplitude and ω is the frequency of the external forcing. While u_1 and u_2 are transversely coupled, v_1 and v_2 are considered to be diffusively inactive along z axis. This allows us to confine ourselves to a minimal coupling scheme for the study of antiresonance. D_u and D_v are the diffusion constants of the components u and v, respectively. We assumed that weak transverse coupling does not affect the diffusion coefficients, so that $D_u(\text{layer } 1) = D_u(\text{layer } 2)$ and $D_v(\text{layer } 1) = D_v(\text{layer } 2)$.

We now denote the uniform steady state (ss) of the coupled system as $(u_{1s}, v_{1s}, u_{2s}, v_{2s})$ and apply perturbation around this state which grows both spatially and temporally in two dimensions. The perturbations $\partial\tilde{u}_i$ and $\partial\tilde{v}_i$ are given by

$$u_i(r,t) = u_{is} + \partial\tilde{u}_i(t,r), \tag{2.5}$$

$$v_i(r,t) = v_{is} + \partial\tilde{v}_i(t,r), \tag{2.6}$$

where $\partial\tilde{u}(t,r) = \int \tilde{u_q}(t)e^{i\vec{q}\,\vec{r}}\,dq$ and $\partial\tilde{v}(t,r) = \int \tilde{v_q}(t)e^{i\vec{q}\,\vec{r}}\,dq$; $|\vec{q}\,| = \sqrt{q_x^2 + q_y^2}$. $\tilde{u_q}(t)$ and $\tilde{v_q}(t)$ are the amplitudes of the perturbation; q_x and q_y are the wave numbers along x and y directions, respectively. For brevity, we omit the q dependence in the subscript of the Fourier wave amplitudes from now on. The linearized dynamics of the two-component system then becomes

$$\dot{\tilde{u}_1} = (f'_{u_1} - q^2D_u)\tilde{u}_1 + f_{v_1}\tilde{v}_1 + \alpha(\tilde{u}_2 - \tilde{u}_1) + (2G_0)\sin(\omega t), \tag{2.7}$$

$$\dot{\tilde{v}_1} = g_{u_1}\tilde{u}_1 + (g'_{v_1} - q^2D_v)\tilde{v}_1, \tag{2.8}$$

$$\dot{\tilde{u}_2} = (f'_{u_2} - q^2D_u)\tilde{u}_2 + f_{v_2}\tilde{v}_2 + \alpha(\tilde{u}_1 - \tilde{u}_2), \tag{2.9}$$

$$\dot{\tilde{v}_2} = g_{u_2}\tilde{u}_2 + (g'_{v_2} - q^2D_v)\tilde{v}_2, \tag{2.10}$$

where

$$f'_{u_i} = \left.\frac{\partial F_i}{\partial u_i}\right|_{ss}, \quad f_{v_i} = \left.\frac{\partial F_i}{\partial v_i}\right|_{ss}, \tag{2.11}$$

$$g_{u_i} = \left.\frac{\partial G_i}{\partial u_i}\right|_{ss}, \quad g'_{v_i} = \left.\frac{\partial G_i}{\partial v_i}\right|_{ss}. \tag{2.12}$$

Abbreviating $(f'_{u_i} - q^2 D_u) = f_{u_i}$ and $(g'_{v_i} - q^2 D_v) = g_{v_i}$ ($i = 1$ or 2), Eqs. (2.7)–(2.10) become

$$\dot{\tilde{u_1}} = f_{u_1}\tilde{u_1} + f_{v_1}\tilde{v_1} + \alpha(\tilde{u_2} - \tilde{u_1}) + (2G_0)\sin(\omega t), \quad (2.13)$$

$$\dot{\tilde{v_1}} = g_{u_1}\tilde{u_1} + g_{v_1}\tilde{v_1}, \quad (2.14)$$

$$\dot{\tilde{u_2}} = f_{u_2}\tilde{u_2} + f_{v_2}\tilde{v_2} + \alpha(\tilde{u_1} - \tilde{u_2}), \quad (2.15)$$

$$\dot{\tilde{v_2}} = g_{u_2}\tilde{u_2} + g_{v_2}\tilde{v_2}. \quad (2.16)$$

Now differentiating both sides of Eq. (2.14) with respect to t and using the expression for $\dot{\tilde{u_1}}$ in the resulting equation, we obtain

$$\ddot{\tilde{v_1}} - g_{v_1}\dot{\tilde{v_1}} - f_{v_1}g_{u_1}\tilde{v_1} = (g_{u_1}\tilde{u_1})(f_{u_1} - \alpha) + g_{u_1}\alpha\tilde{u_2} + (2G_0)\sin(\omega t). \quad (2.17)$$

Elimination of $\tilde{u_1}$ and $\tilde{u_2}$ from Eq. (2.17) using Eq. (2.14) and Eq. (2.16), followed by some rearrangement, yields

$$\ddot{\tilde{v_1}} - (f_{u_1} + g_{v_1} - \alpha)\dot{\tilde{v_1}} + (f_{u_1}g_{v_1} - f_{v_1}g_{u_1})\tilde{v_1} - \alpha\left[g_{v_1}\tilde{v_1} + \frac{g_{u_1}}{g_{u_2}}\dot{\tilde{v_2}} - \frac{g_{u_1}g_{v_2}}{g_{u_2}}\tilde{v_2}\right] = (2G_0)\sin(\omega t). \quad (2.18)$$

Similarly we obtain the equation of $\ddot{\tilde{v_2}}$ as follows:

$$\ddot{\tilde{v_2}} - (f_{u_2} + g_{v_2} - \alpha)\dot{\tilde{v_2}} + (f_{u_2}g_{v_2} - f_{v_2}g_{u_2})\tilde{v_2} - \alpha\left[g_{v_2}\tilde{v_2} + \frac{g_{u_2}}{g_{u_1}}\dot{\tilde{v_1}} - \frac{g_{u_2}g_{v_1}}{g_{u_1}}\tilde{v_1}\right] = 0. \quad (2.19)$$

Now from the condition of stability of the uniform or homogeneous steady state we have the following relations:

$$(f_{u_i} + g_{v_i}) < 0, \quad (2.20)$$

$$(f_{u_i}g_{v_i} - f_{v_i}g_{u_i}) > 0. \quad (2.21)$$

With the following definitions of the constant coefficients: $-(f_{u_i} + g_{v_i} - \alpha) = A_i > 0$ $(\alpha > 0)$, $(f_{u_i}g_{v_i} - f_{v_i}g_{u_i}) = \omega_i^2 > 0$ $(i = 1 \text{ or } 2)$, $\alpha g_{v_1} = E_1$, $\alpha g_{v_2} = E_2$, $\alpha\frac{g_{u_1}}{g_{u_2}} = B_1$, $\alpha\frac{g_{u_2}}{g_{u_1}} = B_2$, $\alpha\frac{g_{u_1}g_{v_2}}{g_{u_2}} = D_1$, and $\alpha\frac{g_{u_2}g_{v_1}}{g_{u_1}} = D_2$. we rewrite Eqs. (2.18) and (2.19) as follows:

$$\ddot{\tilde{v_1}} + A_1\dot{\tilde{v_1}} + \omega_1^2\tilde{v_1} - (B_1\dot{\tilde{v_2}} - D_1\tilde{v_2} + E_1\tilde{v_1}) = (2G_0)\sin(\omega t), \quad (2.22)$$

$$\ddot{\tilde{v_2}} + A_2\dot{\tilde{v_2}} + \omega_2^2\tilde{v_2} - (B_2\dot{\tilde{v_1}} - D_2\tilde{v_1} + E_2\tilde{v_2}) = 0. \quad (2.23)$$

Equations (2.22) and (2.23) are the equations of two coupled linear oscillators, where A_1 and A_2 are the damping constants of the oscillators characterized by their phase space coordinates $(\tilde{v_1}, \dot{\tilde{v_1}})$ and $(\tilde{v_2}, \dot{\tilde{v_2}})$, respectively; ω_1 and ω_2 are the natural frequencies of the oscillators and $B_1(B_2)$, $D_1(D_2)$, and $E_1(E_2)$ inside the brackets include the coupling terms between the two oscillators. The top layer oscillator is subjected to the external periodic forcing of frequency ω. Thus the linearized dynamics of the two-component two identical coupled layers now takes the form of two coupled physical oscillators, which constitute the conventional setup for studying antiresonance.

B. Spatiotemporal antiresonance: Expressions for response amplitude

We begin with the following transformations to change the real variables $(\tilde{v_1}, \dot{\tilde{v_1}})$ and $(\tilde{v_2}, \dot{\tilde{v_2}})$ into the complex variables γ_1 and γ_2 and their conjugates γ_1^* and γ_2^*, respectively, as follows:

$$\gamma_1 = \omega_1\tilde{v_1} + i\dot{\tilde{v_1}}, \quad \gamma_1^* = \omega_1\tilde{v_1} - i\dot{\tilde{v_1}}, \quad (2.24)$$

$$\gamma_2 = \omega_2\tilde{v_2} + i\dot{\tilde{v_2}}, \quad \gamma_2^* = \omega_2\tilde{v_2} - i\dot{\tilde{v_2}}. \quad (2.25)$$

In terms of the complex variables, Eqs. (2.22) and (2.23) can be expressed as follows:

$$\dot{\gamma_1} = -i\omega_1\gamma_1 - \frac{A_1}{2}(\gamma_1 - \gamma_1^*) + \frac{B_1}{2}(\gamma_2 - \gamma_2^*) - \frac{iD_1}{2\omega_2}(\gamma_2 + \gamma_2^*) + \frac{iE_1}{2\omega_1}(\gamma_1 + \gamma_1^*) + G_0 \times 2i\,\sin(\omega t) \quad (2.26)$$

and

$$\dot{\gamma_2} = -i\omega_2\gamma_2 - \frac{A_2}{2}(\gamma_2 - \gamma_2^*) + \frac{B_2}{2}(\gamma_1 - \gamma_1^*) - \frac{iD_2}{2\omega_1}(\gamma_1 + \gamma_1^*) + \frac{iE_2}{2\omega_2}(\gamma_2 + \gamma_2^*). \quad (2.27)$$

Equations (2.26) and (2.27) are then transformed to a frame which is rotating at the driving frequency so that $\gamma_i \to \bar{\gamma_i}e^{-i\omega t}$. This is followed by rotating wave approximation, i.e., we neglect the fast counter-rotating terms which are proportional to $e^{2i\omega t}$ and vanish on averaging over the time scale of our interest. This yields

$$\dot{\bar{\gamma_1}} = (i\Delta_1 - A_1')\bar{\gamma_1} + (B_1' - D_1')\bar{\gamma_2} - G_0, \quad (2.28)$$

$$\dot{\bar{\gamma_2}} = (i\Delta_2 - A_2')\bar{\gamma_2} + (B_2' - D_2')\bar{\gamma_1}, \quad (2.29)$$

where $\Delta_1 = (\omega - \omega_1)$, $\Delta_2 = (\omega - \omega_2)$, $A_1' = (\frac{A_1}{2} - \frac{iE_1}{2\omega_1})$, $A_2' = (\frac{A_2}{2} - \frac{iE_2}{2\omega_2})$, $B_1' = \frac{B_1}{2}$, $B_2' = \frac{B_2}{2}$, $D_1' = \frac{iD_1}{2\omega_2}$, and $D_2' = \frac{iD_2}{2\omega_1}$. Here $\Delta_i = (\omega - \omega_i)$ refers to detuning between the external drive and the natural frequency ω_i of the ith oscillator. Now, in absence of damping, driving, or coupling, the solutions to these equations can be written as

$$\bar{\gamma_i}(t) = \bar{\gamma_i}(0)e^{i\Delta_i t}.$$

This represents a rotation in the complex $\bar{\gamma_i}$ plane with the angular frequency Δ_i. The steady state solutions, $\bar{\gamma_{is}}(s)$, for Eqs. (2.28) and (2.29) can be found setting $\dot{\bar{\gamma_1}} = \dot{\bar{\gamma_2}} = 0$. This condition leads to the complex response functions for the oscillators as follows:

$$\bar{\gamma_{1s}} = \frac{G_0(i\Delta_2 - A_2')}{[(i\Delta_1 - A_1')(i\Delta_2 - A_2')] - [(B_1' - D_1')(B_2' - D_2')]}, \quad (2.30)$$

$$\bar{\gamma_{2s}} = \frac{-G_0(B_2' - D_2')}{[(i\Delta_1 - A_1')(i\Delta_2 - A_2')] - [(B_1' - D_1')(B_2' - D_2')]}. \quad (2.31)$$

Equations (2.30) and (2.31) are the central results of this section. They essentially reflect the behavior of the response amplitude of the components of the coupled reaction-diffusion systems to the frequency of the external sinusoidal drive acting on one component. Theoretical expressions have been derived on the basis of linearization around homogeneous steady states of the system. Two points are now in order. First, it is expected that on varying the frequency of the drive one may realize antiresonance dip at a frequency intermediate between the two resonance maxima of the driven oscillator. To this end we need to work out a specific model of reaction-diffusion system. For the present purpose we have chosen the Gray-Scott reaction [41], which has been the testing ground for various theoretical schemes in nonlinear chemical dynamics. Second, since antiresonance arises due to a destructive interference between external drive and the coupling, it would seem that the stability of the two subsystems differs significantly. In what follows we carry out a detailed numerical simulation of the Gray-Scott system to demonstrate that this differential behavior of stability is remarkably manifested in spatiotemporal patterns in one of the subsystems, while the other goes over to a homogeneous stable state.

III. APPLICATION: NUMERICAL SIMULATION

A. Gray-Scott reaction-diffusion system

The Gray-Scott model is a variant of the cubic autocatalytic model of glycolysis. Basically it considers the reaction $U + 2V \to 3V, V \to P$ in an open flow reactor where U is continuously supplied and the product P is removed. The first reaction represents an autocatalytic process in which two molecules of species V through the interaction with one molecule of species U produce $3V$. The second reaction represents the decay of V into the product P. For a closed system, the irreversibility of the two processes would inevitably transform all reactants into product. However, by constantly feeding the reactor with a uniform supply of species U while removing product and surplus reactants, the far from equilibrium condition can be maintained, allowing for a variety of instabilities and nonlinear dynamic phenomena to unfold. By using a gel reactor medium, convective currents are prevented. The motivation behind choosing the Gray-Scott model is twofold. First, such models are relevant in biological systems, such as the skin of a developing embryo where the supply of reactant could be from the bloodstream, or from cells in an adjacent layer of tissue that continuously generate the needed chemicals with the rates regulated by enzymes. Furthermore, the Gray-Scott model is one of the simplest examples of a stoichiometrically conserved autocatalysis reaction with cubic nonlinearity, having a few parameters. This model reveals a variety of spatial-temporal localized patterns such as stable spots, traveling spots, a mixture of spots and stripes, growing labyrinths, chaotic dynamics, and a continuous process of spot birth through replication and spot death through overcrowding, etc. The second motivation stems from the experimental relevance of the model, e.g., an autocatalytic ferrocyanide-iodate-sulphite (FIS) reaction experiment [42] was performed to exhibit spot self-replication, repeated growth, and annihilation of spots. The chemical reaction kinetics of this FIS reaction is qualitatively similar to that for a modified Gray-Scott model.

After proper rescaling and inclusion of diffusion, the kinetic equations of the two-component two identical Gray-Scott layer problem can be written as

$$\frac{\partial u_1}{\partial t} = -u_1 v_1^2 + s_1(1-u_1) + D_u \nabla^2 u_1 + \alpha(u_2 - u_1) + (2G_0)\sin(\omega t), \tag{3.1a}$$

$$\frac{\partial v_1}{\partial t} = u_1 v_1^2 - (s_1 + k_1)v_1 + D_v \nabla^2 v_1, \tag{3.1b}$$

$$\frac{\partial u_2}{\partial t} = -u_2 v_2^2 + s_2(1-u_2) + D_u \nabla^2 u_2 + \alpha(u_1 - u_2), \tag{3.1c}$$

$$\frac{\partial v_2}{\partial t} = u_2 v_2^2 - (s_2 + k_2)v_2 + D_v \nabla^2 v_2, \tag{3.1d}$$

where u_i and v_i represent the concentrations of species U and V, in top ($i = 1$) and bottom ($i = 2$) layers. k_i is an effective rate constant for decay of V into P, and s_i is the supply rate for the ith layer. The nonlinear terms $u_i v_i^2$ correspond to cubic autocatalytic kinetics as explained earlier for the step $U + 2V \to 3V$. (s_1, k_1) and (s_2, k_2) are the system parameters used to control the spatiotemporal dynamics. D_u and D_v are the diffusion constants for the two species. α is the coupling constant.

We choose the homogeneous steady state $(u_{1s}, v_{1s}, u_{2s}, v_{2s}) = (1, 0, 1, 0)$ for the system, along with two nonzero different sets of (s_i, k_i) for two different layers. For the rest of the treatment the values of the parameters are set as per Ref. [41] as $s_1 = 0.036$, $k_1 = 0.064$, $s_2 = 0.052$, $k_2 = 0.064$, $D_u = 0.00002$, $D_v = 0.00001$, $L_x = 2.5$, and $L_y = 2.5$. The coupling constant and the amplitude of the drive are fixed at $\alpha = 0.002$ and $G_0 = 0.005$, respectively. It is pertinent to note that for the mentioned values of (s_1, k_1) and (s_2, k_2) the spot and stripe patterns are produced, respectively, in absence of coupling and external force. The approximate values of wave vectors can be estimated from the number of nodes of the patterns. For the present purpose we have set $n_x = 15$ and $n_y = 12$. The choice of parameter set [41], in conformity with the homogeneous steady state of the system, assures us that ω_i^2 and A_i ($i = 1, 2$) remain positive.

B. Numerical simulation and spatiotemporal antiresonance

Having specified the parameter set for the Gray-Scott reaction-diffusion system we now return to Eqs. (2.30) and (2.31) for the analysis of theoretical expressions for response amplitudes as a function of frequency of the external drive obtained using linear stability analysis. In Figs. 1(a) and 1(b) we plot the imaginary part of the G_0-scaled response amplitude of the field variable v for the top layer and that the bottom layer, respectively, as a function of frequency. It follows from Fig. 1(a) that the response of the top layer although directly driven is strongly suppressed, almost to zero at around $\omega = 0.07$ in between the two maxima on either sides, whereas the bottom layer exhibits a moderate nonzero response [Fig. 1(b)]. This particular dip in the response curve corresponds to antiresonance for the driven component. The antiresonance frequency implies that at this particular frequency the oscillation of the top layer is completely destroyed,

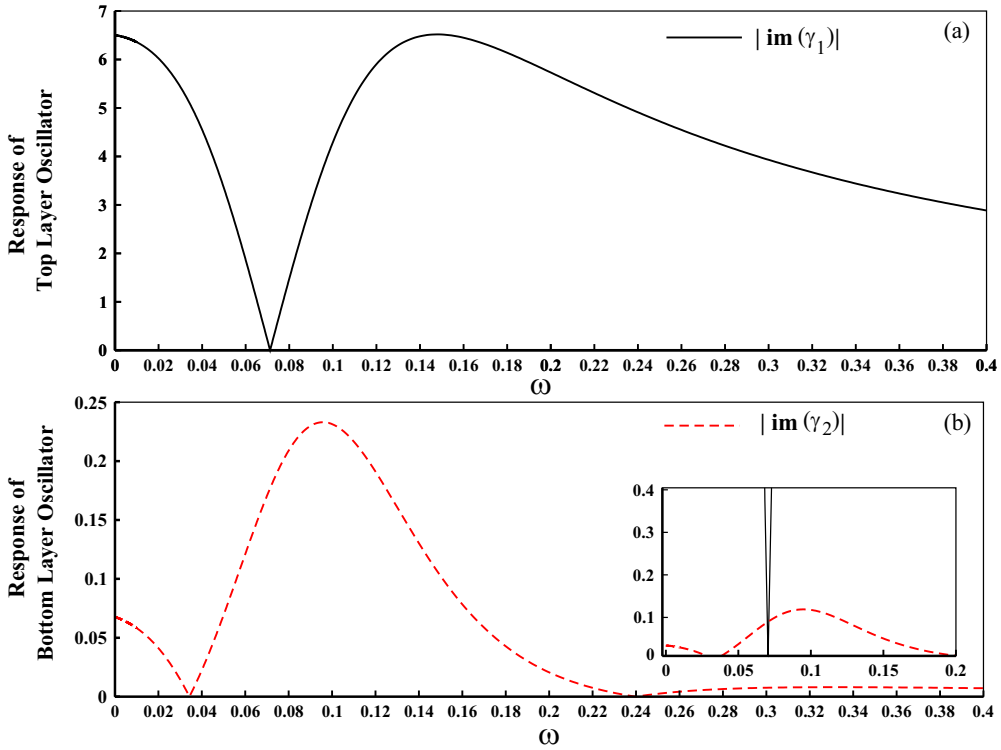

FIG. 1. Linear analysis of spatiotemporal antiresonance in Gray-Scott reaction-diffusion system. (a) The imaginary part of the G_0-scaled response function for v_1 [Eq. (2.30)], where $\bar{\gamma}_{1s}$ for the top layer is plotted against frequency ω of the periodic drive, and (b) the imaginary part of the G_0-scaled response function for v_2 [Eq. (2.31)], where $\bar{\gamma}_{2s}$ for the bottom layer is plotted against the frequency of the periodic drive for the set of parameters as mentioned in the text. [Inset in (b) illustrates the relative magnitude of the two response functions.] Units are arbitrary.

whereas the bottom layer continues to oscillate on its own without any dependence on the first layer.

In what follows in the rest of this section we go beyond linearization and look for the essential consequences of the differential instability in the two layers of the coupled Gray-Scott system using full numerical simulations of Eqs. (3.1a)–(3.1d) in the presence of the external periodic drive $2G_0 \sin(\omega t)$ on the top layer. The numerical integration of the partial differential equations was done using the Euler central difference scheme over (250×250) discrete grid points in two dimensions for each of the two layers for each component in the system for the set of parameters as mentioned before. The spatial resolution for the space coordinate was set as $\Delta x = \Delta y = 0.01$ for each case and depending on the time scale of the sinusoidal drive the time increment dt was chosen. For a long time period, say for $\omega = 10^{-8}$, dt was chosen as 1.0, while for a relatively shorter time period, such as for $\omega = 0.2$, dt was set as 0.1. In all cases stability and convergence were checked against the choice of time steps of integration. Initially all the nodes of the grid were kept at the steady state: $(u_{1s}, v_{1s}, u_{2s}, v_{2s}) = (1, 0, 1, 0)$. This was followed by a perturbation of a (20×20) mesh area at the middle of the grids of both layers and finally by 1% random noise to all the nodes (250×250) of both layers to break the square symmetry. Numerical integration was carried out using periodic boundary conditions, over around 10^7 time units. The results are displayed in Figs. 2–5.

As per linear analysis the antiresonance appears at around $\omega \approx 0.07$. We therefore begin our numerical simulation of the coupled Gray-Scott system over a wide range of frequencies centering at 0.07 from $\omega = 10^{-9}$ to $\omega = 1.0$. When $\omega = 0$ the coupled system exhibits spatiotemporal patterns for both the layers. The region of antiresonance should lie approximately around $\omega \approx 0.07$. In this region the top driven layer is expected to stop oscillating while the undriven bottom layer continues to oscillate, making the upper layer homogeneous and the bottom layer a nonstationary patterned state in the long time limit. However, in the lower and higher frequency regime on either side of the antiresonance region, both layers should exhibit patterns with their usual oscillations. To highlight the temporal oscillations in terms of field variables we have specifically chosen the (125th×125th) node of the top and bottom layers for v_1 and v_2, respectively. We now show the spatiotemporal evolution of the top and bottom layers in terms of v_1 and v_2 for four cases and we have divided them into the following three regimes.

(i) Low frequency regime

The spatiotemporal evolution of the dynamics of the coupled system is now displayed in Fig. 2 for $\omega = 10^{-8}$ up to $\sim 1.5\times10^7$ time units. The top panel in Fig. 2(a) shows the time evolution of the oscillations of the field variables v_1 (in solid-black line) and v_2 (in red-dashed line) at the (125th×125th) node. The middle panel in Figs. 2(b)–2(e) and the bottom panel in Figs. 2(f)–2(i) shows the evolution of the pattern of the top layer v_1 and the bottom layer v_2, respectively, at $t = 10^4$, 10^5, 10^6, and 10^7 time units. Thus

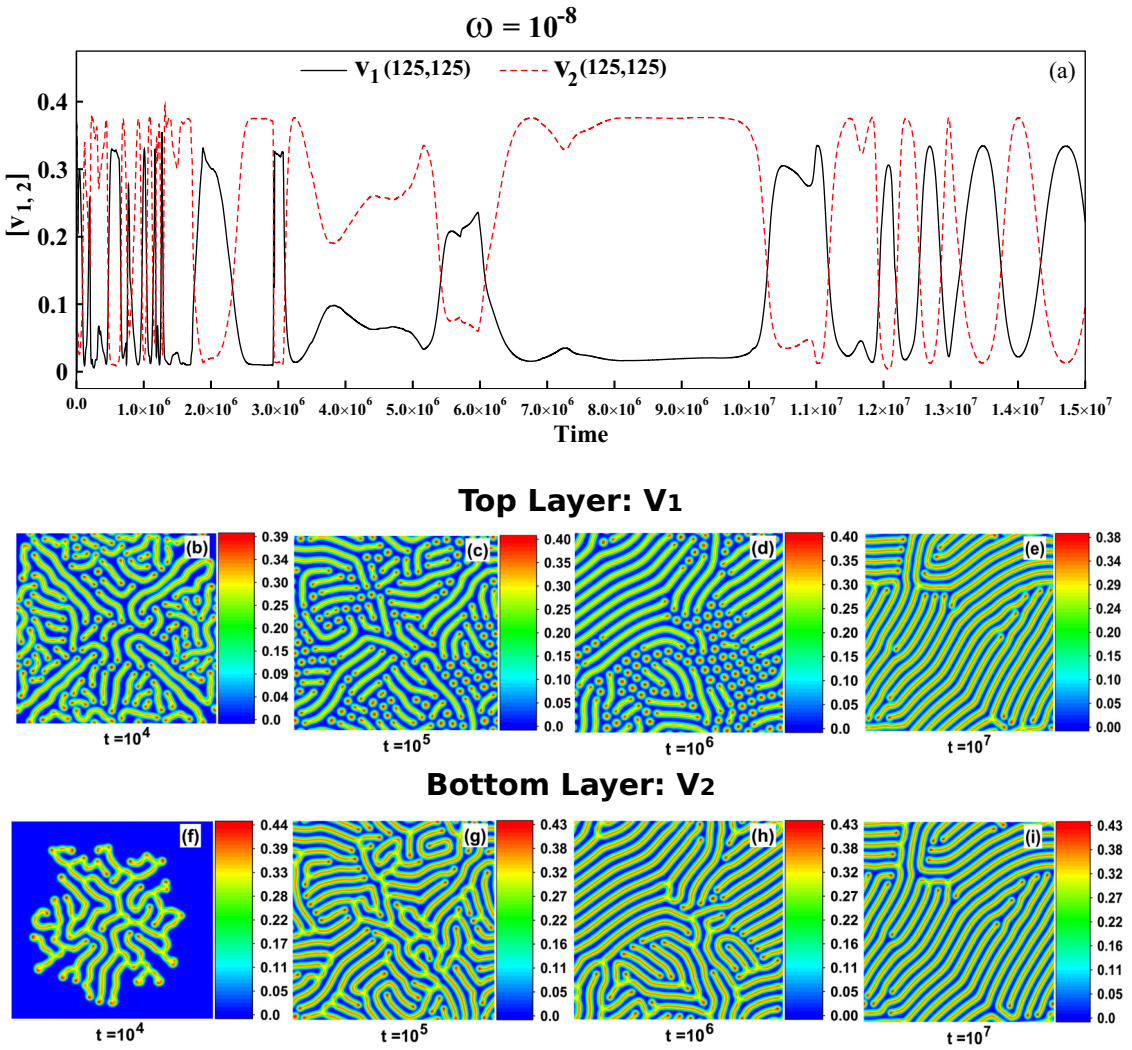

FIG. 2. Numerical simulation of the periodically driven coupled Gray-Scott reaction-diffusion system [Eq. (3.1)] for the parameter set mentioned in the text and time increment $dt = 1.0$: low frequency regime, $\omega = 10^{-8}$. Top panel: (a) sustained oscillation of concentration of v_1 (shown by solid-black line) and concentration of v_2 (shown by red-dashed line) at (125th×125th) node of the top and bottom layers, respectively, plotted as function of time up to t = 1.5×10^7 time units.Middle panel: concentration profile of v_1 in top layer at time units (b) $t = 10^4$, (c) $t = 10^5$, (d) $t = 10^6$, and (e) $t = 10^7$, in x and y directions. Bottom panel: concentration profile of v_2 in bottom layer at time units (f) $t = 10^4$, (g) $t = 10^5$, (h) $t = 10^6$, and (i) $t = 10^7$, in x and y directions. Both layers exhibit nonstationary patterns. (Units arbitrary.)

from Fig. 2 it is immediately apparent that both the reacting components in top and bottom layers continue to oscillate temporally and the mixing of the patterns is observed. We have obtained qualitatively similar features for the frequency ranging from as low as $\omega = 10^{-9}$ to $\omega =\sim 10^{-6}$. This region refers to the left side of the antiresonance dip at $\omega = 0.07$ in Fig. 1, as predicted by the linear analysis.

(ii) Intermediate frequency regime; spatiotemporal antiresonance

The simulation is now extended to the intermediate frequency domain. In Figs. 3 and 4, we have presented the results of the spatiotemporal evolution for the driving frequency $\omega = 10^{-5}$ and 0.08, respectively, keeping all other parameters fixed. It is evident from the temporal profiles of the field variables at the chosen node in Figs. 3(a) and 4(a) that, in the top driven layer, v_1 (shown using black-dot-dashed line) stops oscillating within a very short time, while v_2 in the bottom undriven layer undergoes sustained oscillation. This is clearly reflected in Figs. 3(b)–3(e) and 4(b)–4(e), which show that after some spatiotemporal transients the system settles down to a homogeneous steady state. As the frequency increases from 10^{-5} to 0.08 the disappearance of the transient patterns in the top layers becomes faster. The reaction components in the bottom layers in Figs. 3(f)–3(i) and 4(f)–4(i) continue to oscillate and generate patterns. The difference in stability of the two layers thus induces spatiotemporal antiresonance in the coupled system and the qualitative prediction obtained from the linear analysis is corroborated. Interestingly, with increasing frequency the temporal oscillation of the reaction component in the bottom layer, v_2, shows a low amplitude high frequency oscillation modulating natural oscillation

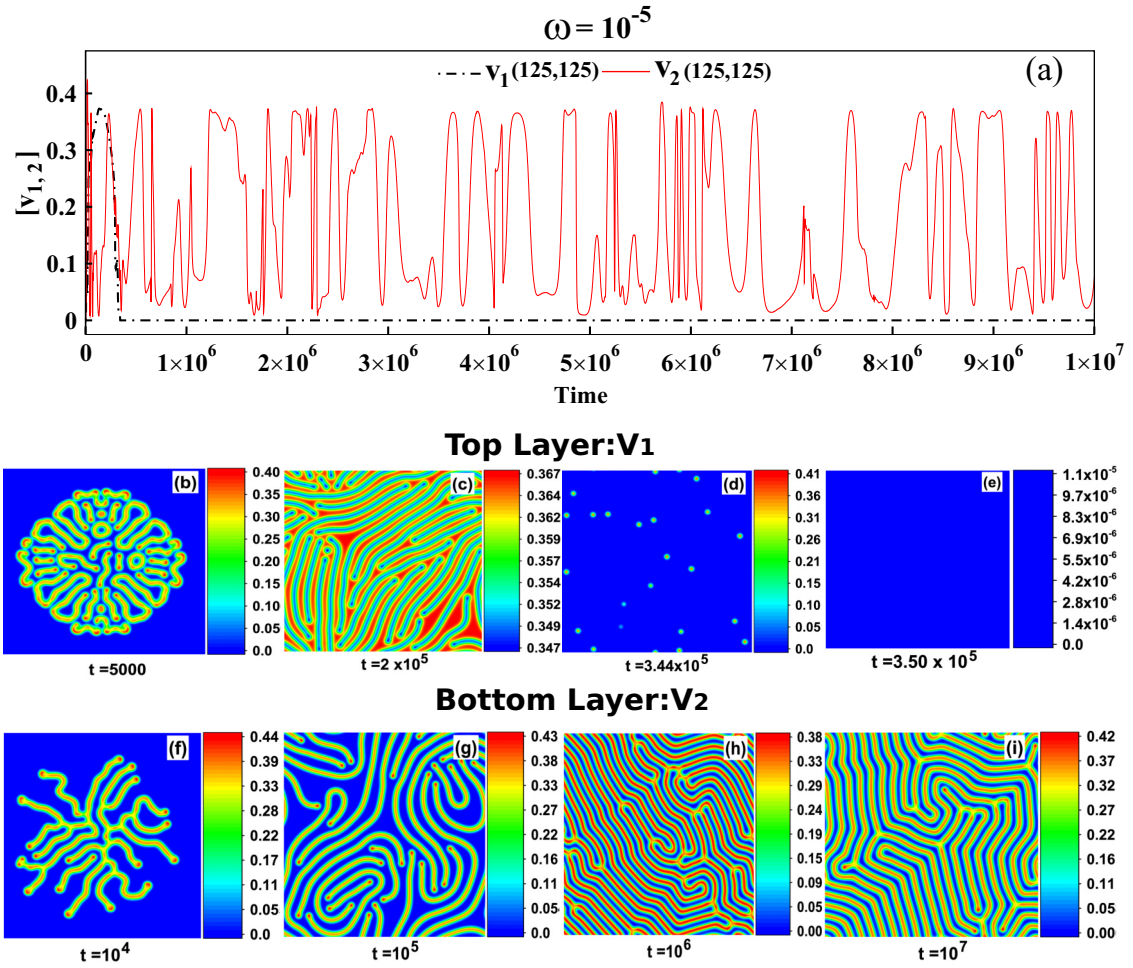

FIG. 3. Numerical simulation of periodically driven coupled Gray-Scott reaction-diffusion systems [Eq. (3.1)] for the parameter set mentioned in the text and time increment $dt = 1.0$: intermediate frequency or antiresonance regime, $\omega = 10^{-5}$. Top panel: (a) collapse of oscillation of concentration v_1 (shown by dot-dashed-black line) to the steady state and sustained oscillation of concentration v_2 (shown by red-solid line) at the (125th×125th) node of the top and bottom layers, respectively, plotted as a function of time up to $t = 10^7$ time units. Middle panel: concentration profile of v_1 in top layer at time units (b) $t = 5000$, (c) $t = 2\times10^5$, (d) $t = 3.44\times10^5$, and (e) $t = 3.50\times10^5$, in x and y directions. The top layer settles down to a homogeneous steady state. Bottom panel: concentration profile of v_2 in bottom layer at time units (f) $t = 10^4$, (g) $t = 10^5$, (h) $t = 10^6$, and (i) $t = 10^7$, in x and y directions. The bottom layer exhibits spatiotemporal patterns. (Units arbitrary.)

around the steady state as evident from the inset of the top panel of Fig. 4(a).

Although the linear stability analysis predicts a sharp antiresonance dip when the frequency of the external periodic drive is varied, the spatiotemporal antiresonance as observed in numerical simulation persists over a wider range of frequencies, e.g., from $\omega =\sim 10^5$ to $\omega =\sim 0.1$. The observation of antiresonance requires a critical adjustment of the coupling and the frequency of external drive, while fine-tuning is required for linear systems since the frequency of a linear system does not depend on its amplitude of oscillation. In full scale simulation of the nonlinear model, however, such fine-tuning of frequency is not essential since the amplitude of oscillation takes care of readjustment of frequency with coupling and antiresonance appears over a range of frequency. An immediate consequence is that the region of differential stability of the two subsystems gets widened. In order to reduce the number of parameters and to have a clear guideline from the linear analysis we have confined ourselves to a minimal model of coupling. We mention, in passing, that going beyond the minimal model by considering coupling between v_1 and v_2 necessarily does not preclude the possibility of observation of spatiotemporal antiresonance but correspondence to linear analysis by casting the coupled reaction-diffusion systems into a coupled oscillator problem turns out to be extremely cumbersome.

(iii) High frequency regime

Figure 5 depicts the result of numerical simulation for $\omega = 0.2$. In this frequency range the reaction components in both upper and bottom layers v_1 and v_2 execute sustained oscillation in the long time limit as evident from Fig. 5(a). Concurrently, both v_1 and v_2 exhibit spatiotemporal patterns

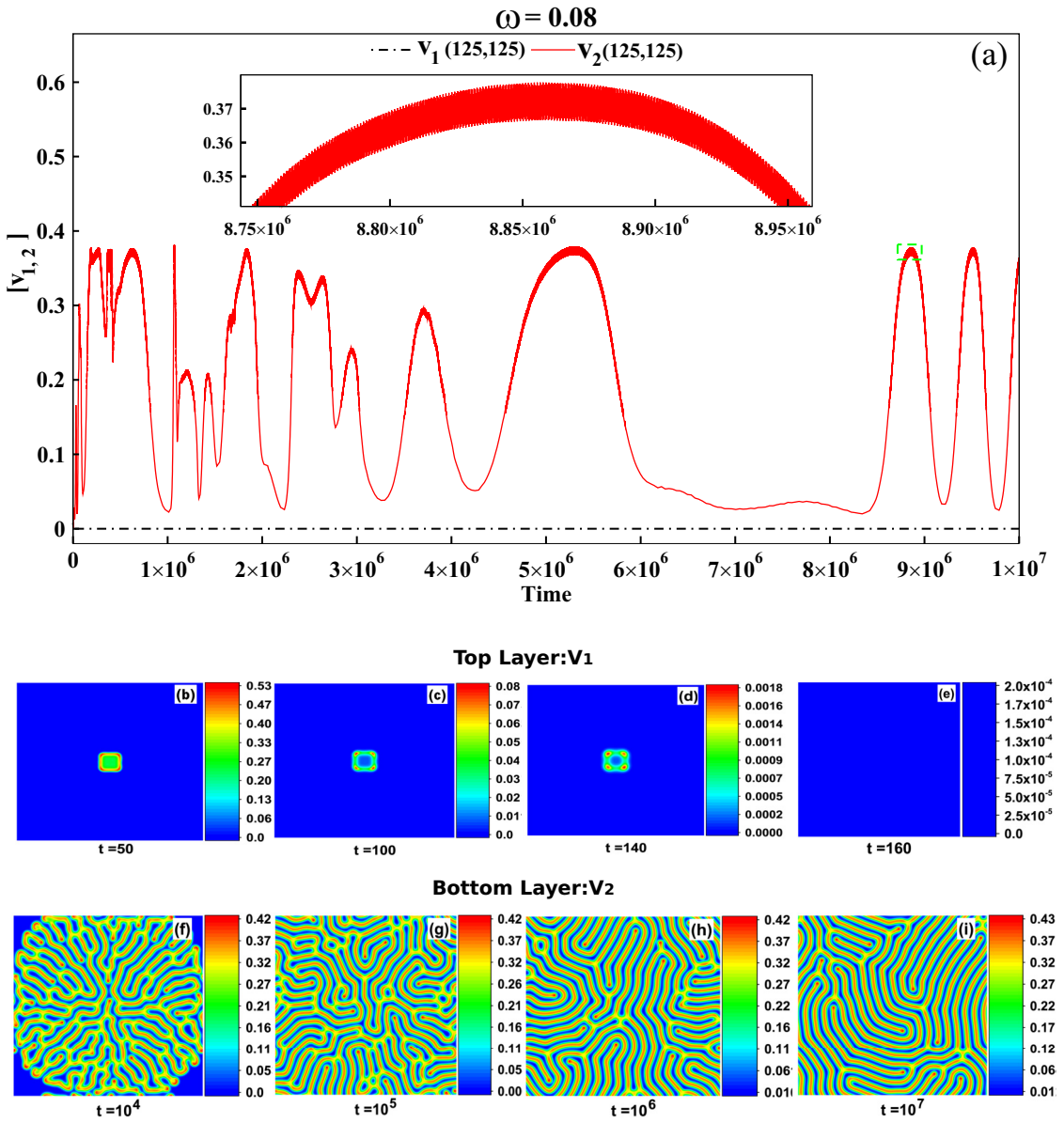

FIG. 4. Same as in Fig. 3 but for $\omega = 0.08$ and time increment $dt = 0.1$. Middle panel: concentration profile of v_1 in top layer at time units (b) $t = 50$, (c) $t = 100$, (d) $t = 140$, and (e) $t = 160$, in x and y directions. Inset in (a) shows the low amplitude high frequency oscillation of the marked area shown with dotted-green box. (Units arbitrary.)

as shown in Figs. 5(b)–5(e) and 5(f)–5(i). In this high frequency regime the coupling remains unaffected and external drive induces oscillations and spatiotemporal patterns. We have observed that for the range starting from $\omega = \sim 0.2$ to as high as $\omega = 1.0$ one observes spatiotemporal patterns in both layers.

IV. CONCLUSION

In this work we have carried out a theoretical investigation of the spatiotemporal antiresonance in a two layer of transversely coupled reaction-diffusion systems in the presence of external periodic forcing to one of the constituents. It has been shown that the linearized dynamics around the homogeneous steady state can be cast into a coupled oscillator problem. This allows us to derive the general analytical expressions for amplitude-frequency response functions for each of the subsystems within the rotating wave approximation. An explicit example with the Gray-Scott model has been worked out to demonstrate a sharp fall of response amplitude of the driven reaction-diffusion component at a particular driving frequency, whereas the other component shows nonzero response at the frequency. As the physical origin of antiresonance lies on the destructive interference of coupling and driving, it is imperative that this interference gives rise to differential spatiotemporal instability in the two layers of the coupled system. Our numerical simulation clearly reveals that this instability results in nonstationary spatial patterns in the undriven subsystem, while the driven subsystem goes over to a quiescent state, i.e., a homogeneous stable state. We

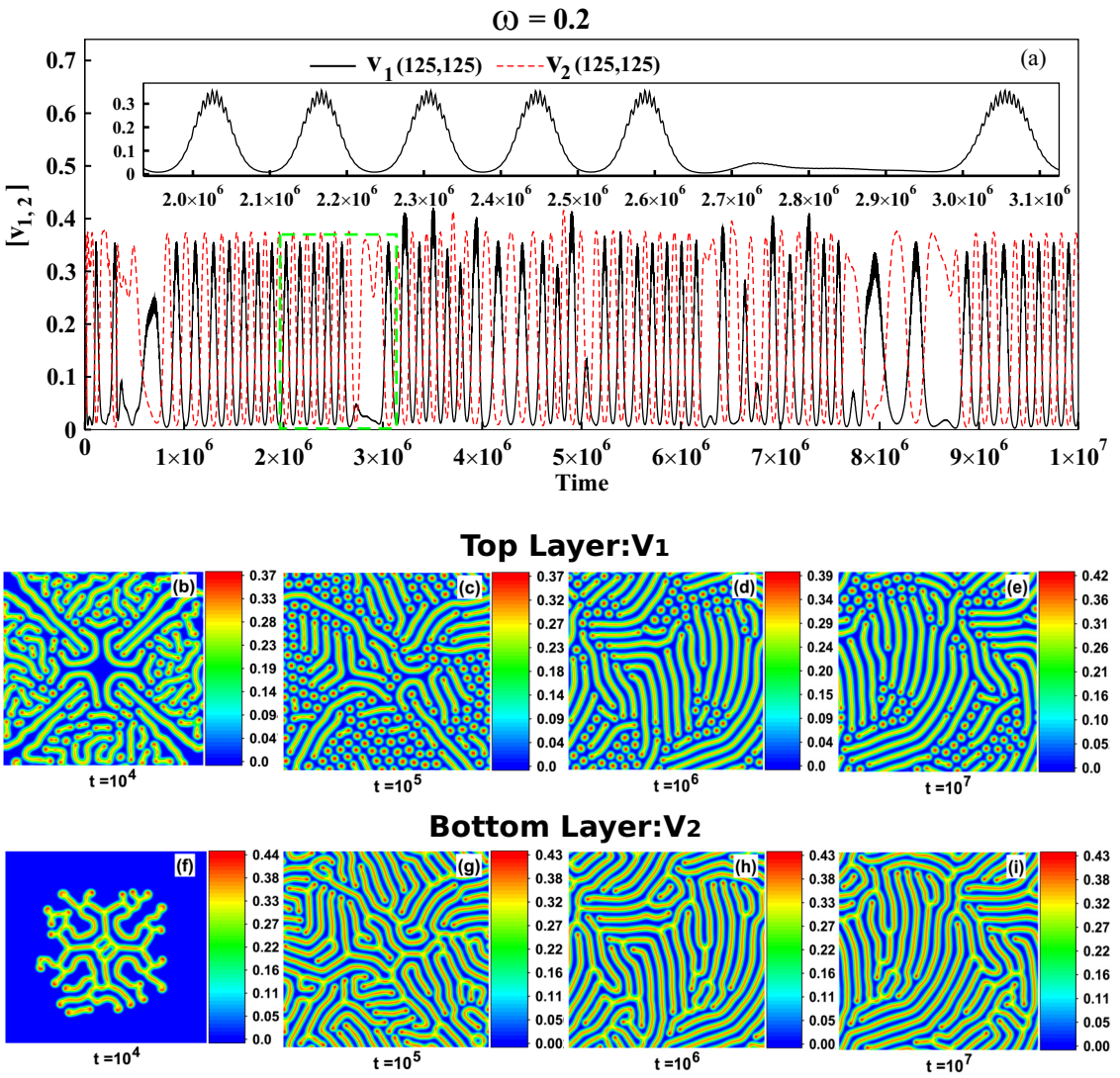

FIG. 5. Numerical simulation of periodically driven Gray-Scott reaction-diffusion systems [Eq. (3.1)] for the parameter set mentioned in the text and time increment $dt = 0.1$: high frequency regime, $\omega = 0.2$. Top panel: (a) sustained oscillation of concentration of v_1 (shown by solid-black line) and concentration of v_2 (shown by red-dashed line) at (125th×125th) node of the top and bottom layers, respectively, plotted as function of time up to 10^7 time units. Middle panel: concentration profile of v_1 in top layer at time units (b) $t = 10^4$, (c) $t = 10^5$, (d) $t = 10^6$, and (e) $t = 10^7$, in x and y directions. Bottom panel: concentration profile of v_2 in bottom layer at time units (f) $t = 10^4$, (g) $t = 10^5$, (h) $t = 10^6$, and (i) $t = 10^7$, in x and y directions. Both layers exhibit nonstationary patterns. Inset in (a) shows the low amplitude high frequency oscillation of the marked area shown with dotted-green box. (Units arbitrary.)

have considered a minimal model of transversal coupling, which implies that diffusive motion of one component of the reaction-diffusion system is much slower compared to the other. Another requirement is the periodic driving of one of the two components of the system. This can be implemented by suitable adjustment of the substrate injection rate into the chosen layer. Although the linear analysis predicts a sharp antiresonance dip in between two resonance maxima, our full scale numerical simulation reveals a range of frequencies for which the antiresonance is observed. We believe that this spatiotemporal antiresonance as observed here is generic for a class of coupled reaction-diffusion systems which can be suitably tuned to control coupling and external drive to realize the phenomenon under appropriate conditions.

ACKNOWLEDGMENTS

K.P. gratefully acknowledges the financial support from DBT-RA Program in Biotechnology and Life Sciences, Government of India. Thanks are due to the University Grants Commission, Government of India for a fellowship (S.P.) and Department of Science and Technology, under Government of India, for a J. C. Bose National Fellowship (D.S.R.) under Grant No. SB/S2/JCB-030/2015 for partial financial support.

[1] D. J. Ewins, *Modal Testing: Theory and Practice* (Wiley, New York, 1984).

[2] S. Belbasi, M. E. Foulaadvand, and Y. S. Joe, Am. J. Phys. **82**, 32 (2014).

[3] R. Jothimurugan, K. Thamilmaran, S. Rajasekar, and M. A. F. Sanján, Nonlin. Dyn. **83**, 1803 (2015).

[4] S. Rajasekar and M. A. F. Sanjuán, *Nonlinear Resonances*, Springer Series in Synergetics (Springer, Basel, Switzerland, 2016).

[5] P. Sarkar and D. S. Ray, Phys. Rev. E **99**, 052221 (2019).

[6] F. Wahl, G. Schmidt, and L. Forrai, J. Sound Vib. **219**, 379 (1999).

[7] K. Abirami, S. Rajasekar, and M. A. F. Sanjuán, Pramana J. Phys. **81**, 127 (2013); P. Rice and R. Breacha, Opt. Commun. **126**, 230 (1996).

[8] M. I. Dykman and M. V. Fistul, Phys. Rev. B **71**, 140508(R) (2005).

[9] C. Sames, H. Chibani, C. Hamsen, P. A. Altin, T. Wilk, and G. Rempe, Phys. Rev. Lett. **112**, 043601 (2014).

[10] S. Jeyakumari, V. Chinnathambi, S. Rajasekar, and M. A. F. Sanjuán, Phys. Rev. E **80**, 046608 (2009).

[11] Y. Liu, Y. Zheng, W. Gong, and T. Lu, Phys. Lett. A **360**, 154 (2006).

[12] B. Lysyansky, O. V. PopoVych, and P. A. Tass, J. Neural Eng. **8**, 036019 (2011).

[13] K. Uchino, Smart Mater. Struct. **7**, 273 (1998).

[14] W. Dámbrogio and A. Fregolent, J. Sound Vib. **236**, 227 (2000); K. Jones and J. Turcotte, *ibid.* **252**, 717 (2002); D. Hanson, T. P. Waters, D. J. Thompson, R. B. Randall, and R. A. J. Ford, Mech. Syst. Signal Process. **21**, 74 (2007); J. E. Mottershead, *ibid.* **12**, 591 (1998).

[15] W. B. Jeong, W. S. Yoo, and J. Y. Kim, KSME Int. J. **17**, 1732 (2003); N. C. Lien and G. C. Yao, J. Chin. Inst. Eng. **24**, 45 (2001).

[16] D. M. Pozar, in *Microwave Engineering* (Wiley, New York, 2004), p. 275; C. W. Sayre, in *Complete Wireless Design*, 2nd ed. (McGraw-Hill Professional, New York, 2008), p. 4.

[17] A. F. McKinley, T. P. White, I. S. Maksymov, and K. R. Catchpole, J. Appl. Phys. **112**, 094911 (2012); S. Lin and J. Xu, Sensors **17**, 329 (2017).

[18] A. Renault, O. Thomas, and H. Mahé, Mech. Syst. Signal Process. **116**, 963 (2019).

[19] P. Sjövall and T. Abrahamsson, Mech. Syst. Signal Process. **22**, 15 (2008).

[20] Z. Agur, J. Theor. Med. **1**, 237 (1998).

[21] H. G. Rotstein, J. Comput. Neurosci. **43**, 35 (2017).

[22] J. Bai *et al.*, Nat. Mater. **18**, 364 (2019).

[23] D. Plankensteiner, C. Sommer, H. Ritsch, and C. Genes, Phys. Rev. Lett. **119**, 093601 (2017).

[24] I. R. Epstein, I. B. Berenstein, M. Dolnik, V. K. Vanag, L. Yang, and A. M. Zhabotinsky, Philos. Trans. R. Soc. London A **366**, 397 (2008); A. M. Turing, Philos. Trans. R. Soc. London B **237**, 37 (1952).

[25] I. Prigogine and R. Lefever, J. Chem. Phys. **48**, 1695 (1968); M. Tlidi, M. G. Clerc, and K. Panajotov, Philos. Trans. R. Soc. A **376**, 20180114 (2018); **376**, 20180276 (2018).

[26] R. A. Barrio, C. Varea, J. L. Aragon, and P. K. Maini, Bull. Math. Biol. **61**, 483 (1999).

[27] L. F. Yang, M. Dolnik, A. M. Zhabotinsky, and I. R. Epstein, Phys. Rev. Lett. **88**, 208303 (2002).

[28] A. Gierer and H. Meinhardt, Kybernetik **12**, 30 (1972).

[29] K. M. Page, P. K. Maini, and N. A. M. Monk, Physica D **202**, 95 (2005).

[30] C. P. Schenk, M. Or-Guil, M. Bode, and H. G. Purwins, Phys. Rev. Lett. **78**, 3781 (1997).

[31] I. Berenstein, M. Dolnik, L. Yang, A. M. Zhabotinsky, and I. R. Epstein, Phys. Rev. E **70**, 046219 (2004).

[32] D. G. Miguez, M. Dolnik, I. R. Epstein, and A. P. Muñuzuri, Phys. Rev. E **84**, 046210 (2011).

[33] L. Yang and I. R. Epstein, Phys. Rev. Lett. **90**, 178303 (2003); Phys. Rev. E **69**, 026211 (2004); L. Ji and Q. S. Li, J. Chem. Phys. **123**, 94509 (2005); F. C. Liu, Y. F. He, and Y. Y. Pan, Commun. Theor. Phys. **53**, 971 (2010); A. J. Catllá, A. McNamara, and C. M. Topaz, Phys. Rev. E **85**, 026215 (2012).

[34] L. Ji and Q. S. Li, Chem. Phys. Lett. **424**, 432 (2006).

[35] B. Kaoui, M. Lauricella, and G. Pontrelli, Comput. Biol. Med. **93**, 149 (2018); E. J. Carr and G. Pontrelli, Math. Biosci. **303**, 1 (2018); S. McGinty, S. Mckee, R. M. Wadsworth, and C. Mccormick, SIAM J. Appl. Math. **73**, 2004 (2013).

[36] V. K. Vanag and I. R. Epstein, Phys. Rev. Lett. **90**, 098301 (2003).

[37] S. Kar and D. S. Ray, Europhys. Lett. **67**, 137 (2004); S. S. Riaz, S. Dutta, S. Kar, and D. S. Ray, Eur. Phys. J. B **47**, 255 (2005); S. S. Riaz, S. Banarjee, S. Kar, and D. S. Ray, *ibid.* **53**, 509 (2006); P. Ghosh and D. S. Ray, J. Chem. Phys. **135**, 104112 (2011); D. Das and D. S. Ray, Phys. Rev. E **87**, 062924 (2013); S. Ghosh and D. S. Ray, J. Chem. Phys. **143**, 124901 (2015); Phys. Rev. E **93**, 032209 (2016); S. Paul, S. Ghosh, and D. S. Ray, *ibid.* **94**, 062217 (2016).

[38] L. Yang, M. Dolnik, A. M. Zhabotinsky, and I. R. Epstein, Chaos **16**, 037114 (2006).

[39] M. Dolnik, A. M. Zhabotinsky, and I. R. Epstein, Phys. Rev. E **63**, 026101 (2001); L. Kuhnert, K. I. Agladze, and V. I. Krinsky, Nature (London) **337**, 244 (1989); O. Steinbock, V. Zykov, and S. C. Muller, *ibid.* **366**, 322 (1993); S. Kadar, T. Amemiya, and K. Showalter, J. Phys. Chem. A **101**, 8200 (1997).

[40] S. Ghosh and D. S. Ray, Eur. Phys. J. B **88**, 180 (2015); H. Larralde, Y. Lereah, P. Trunfio, J. Dror, S. Havlin, R. Rosenbaum, and H. E. Stanley, Phys. Rev. Lett. **70**, 1461 (1993); L. Lizana, Z. Konkoli, and O. Orwar, J. Phys. Chem. B **111**, 6214 (2007).

[41] J. E. Pearson, Science **261**, 189 (1993).

[42] K. Lee, W. D. McCormick, J. E. Pearson, and H. L. Swinney, Nature (London) **369**, 215 (1994).